Exp Fluids
DOI 10.1007/s00348-007-0374-3

RESEARCH ARTICLE

Tracking the free surface of time-dependent flows: image processing for the dam-break problem

Steve Cochard · Christophe Ancey

Received: 20 November 2006 / Revised: 1 August 2007 / Accepted: 1 August 2007

Abstract The dam-break problem (i.e., the sudden release of a given volume of fluid down a slope) has attracted a great deal of attention from mechanicians and physicists over the past few years, with particular interest devoted to the free-surface profile and the spreading rate. Experimentally, impediments to accurate measurements of the free-surface evolution are numerous because of the significant variations in its curvature and velocity. To accurately measure the surge's free-surface variations with time, we have developed a new imaging system, consisting of a digital camera coupled with a synchronized micro-mirror projector. The object's surface is imaged into a camera and patterns are projected onto the surface under an angle of incidence that differs from the imaging direction. From the deformed pattern recorded by the camera, the phase can be extracted and, by using unwrapping algorithms, the height can be computed and the free surface reconstructed. We were able to measure the free surface of the flow to within 1 mm over a surface of 1.8×1.1 m^2. Although the techniques used in our system are not new when taken individually, the system in its entirety is innovative and more efficient than most methods used to-date in practical applications.

S. Cochard (✉) · C. Ancey
Ecole Polytechnique Fédérale de Lausanne,
EPFL - ENAC - ICARE - LHE, Station 18/GC A1-391,
1015 Lausanne, Switzerland
e-mail: steve.cochard@a3.epfl.ch

C. Ancey
e-mail: christophe.ancey@epfl.ch

1 Introduction

The shallow-water equations were originally worked out by Saint Venant (1871) to compute flood propagation along rivers. They were gradually adapted to strongly time-dependent flows such as waves induced by a dam break (Ritter 1892). A growing number of models based on the shallow-water equations are currently being used to describe natural flows such as flash floods (Hogg and Pritchard 2004), floods with sediment transport (Pritchard 2005), snow avalanches (Bartelt et al. 1999), debris flows (Iverson 1997; Huang and García 1997), lava flows (Griffiths 2000), subaqueous avalanches (Parker et al. 1986), and so on. In the derivation of these models, a number of assumptions are used, the most important of which are: the long-wave approximation (no significant curvature of the free surface), hydrostatic pressure, blunt velocity profile, and no change in the bulk composition or rheology. Furthermore, in these models, the bottom shear stress is computed using either empirical expressions (e.g., Chézy friction) or non-Newtonian constitutive equations, with the difficult question of parameter estimation remaining. Given the number of approximations and assumptions needed to obtain these models, one can legitimately be suspicious of their reliability and performance.

Essentially, our idea was to test the shallow-flow equations under extreme conditions in a well-controlled environment—the laboratory—where both the initial and boundary conditions are prescribed. Here, 'extreme conditions' mean that we focus our attention on time-dependent flows (surges with a front) mobilizing Newtonian or non-Newtonian fluids, experiencing different stages from release to run-out: acceleration (balance between inertia and pressure gradient), a nearly fully developed regime (flow at equilibrium), and deposition (predominance of dissipation

processes). The preliminary experiments presented here were run with viscoplastic materials.

The objective of this paper is to describe the experimental procedures used for reconstructing three-dimensional, time-dependent profiles of flow depth. To give the reader an overview of the experimental setting, we will describe the experimental facilities and procedures that we use to generate surges down an inclined plane (see Sect. 2). Tracking the free surface of a rapid surge remains delicate, especially when speed and accuracy are sought. Various techniques have been used in recent years. For instance, Iverson et al. (2004) used parallel laser sheets to reconstruct rapid granular avalanches down irregular topography; Pouliquen and Forterre (2002) used a Moiré technique, while Eaket et al. (2005) employed high-speed stereoscopy for the same purpose.

Here, we will present an image-processing technique based on pattern projection. In itself, the technique is not new (e.g., see Desmangles 2003), but we think that the particular application described herein is innovative given the number of technical problems that must be sorted out for it to be operated in dam-break experiments. Various strategies can be contemplated to reconstruct three-dimensional, time-dependent free surfaces. Pattern projection turns out to be very convenient in terms of cost, robustness, accuracy, and versatility. A key point concerns the computation of flow depth. In Sects. 3.2 and 3.3, we will show how to use fringe deformation to reconstruct a three-dimensional profile. The basic idea underpinning our developments is that in terms of signal processing, free-surface variations entail fringe deformations, viz phase shift and, possibly, amplitude modulation. Section 4 is devoted to phase mapping; the different algorithms used will be outlined there. Usually, a phase map is calculated using a three- or four-image algorithm (as described in Sect. 4.1); for fast flows, we use a one-image algorithm (see Sects. 4.2 and 4.3). The phase, defined in the interval $[0, 2\pi)$, is then unwrapped as explained in Sect. 5. Back computation (recovering flow depth from phase shift) will be presented in Sect. 6: we will show how the flow depth can be deduced from the unwrapped phase signal. Finally, we will give an example of its application in Sect. 7.

2 Facility and procedures

2.1 Overview

Figure 1 gives a view of the experimental setup, while Fig. 2 shows the upper inclined plane, the reservoir, and the gate. Typically, an experiment is run as follows. An amount of fluid is placed in a reservoir at the top of an inclined plane. The fluid is suddenly released by opening the dam's sluice gate. Using a high-speed digital camera,

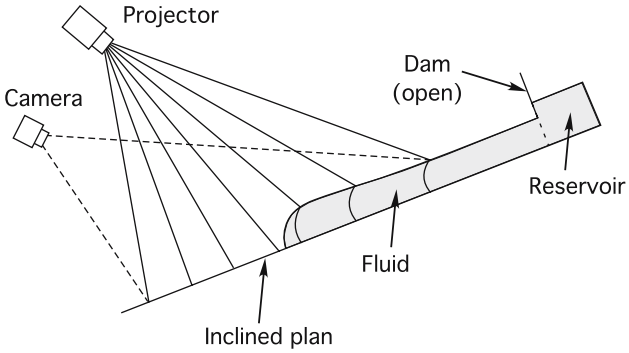

Fig. 1 The experimental setup and the measurement system

Fig. 2 View on the sluice gate and the reservoir at the channel inlet

we then record how a fringe pattern projected on the flow surface is deformed, which makes it possible to measure the flow depth at any place on the surface.

More specifically, our system works in the following way. A micro-mirror projector projected periodic fringe patterns of incoherent light onto the surface, as explained in Sect. 3.3. We placed the digital camera above the flow, but with an incidence angle that differed from the projection angle. This camera recorded how the projected fringes were deformed by the free surface. In terms of signal processing, fringe deformation is equivalent to a phase offset, which can be shown to be directly proportional to the local flow thickness. Thus, measuring flow depth boils down to measuring phase offset.

2.2 Experimental facility

The facility was made up of a metal frame supporting an inclined plane, a horizontal plane (run-out zone), and a reservoir, as sketched in Fig. 3. This structure was 6 m long, 1.8 m wide, and 4 m high. The 4-m-long aluminium inclined plane could be inclined from 0° to 45°, powered by an electric motor. Its position was accurately imposed

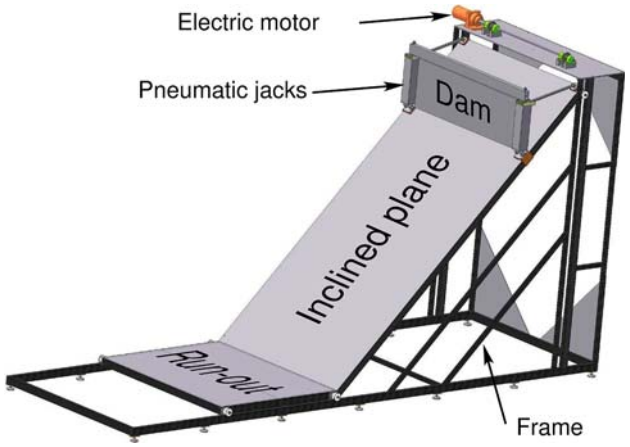

Fig. 3 Schematic perspective of the facility

using a laser-meter to within 1 mm, which means that the accuracy of slope inclination was on the order of 0.1°. The 6-mm-thick aluminium plate was supported by a frame made of profiled aluminium beams (of section 40×80 mm^2) to ensure rigidity.

Different PVC channels were positioned on the inclined plane in order to limit the lateral spreading of the fluid in the cross-stream direction. As for the inclined plane, the channels could be inclined from 0° to 45° and could have different widths and shapes.

A PVC reservoir of varying volume and shape was positioned at the top of the inclined plane behind the dam wall. The maximum capacity of the reservoir was 120 kg. The dam wall was composed of a 1.6×0.8 m^2 ultralight carbon plate. Two pneumatic jacks opened the sluice gate within 0.8 s. An ultralight dam wall was needed to reduce dam-wall inertia, plane vibration, and jerk. The two jacks were quickly raised by injecting air pressured at 7 MPa. Two electromagnetic sensors were located at the tip of each jack to control its position and reset the clock.

The run-out plane had two functions: first—and this is the most important point—the flowing material was forced to undergo a transition from a flow regime to a deposition (run-out) regime. Second, it collected the fluid flowing from the inclined plane, which made the cleaning operations easier. The 1.5-m-long, 1.8-m-wide run-out plane was maintained in a horizontal position and was connected to the inclined plane by a sealing plastic band. The projector and the camera were fixed on another frame, which was independent of the main frame.

2.3 Experimental procedure

A typical experimental run can be split into four stages.

1. The fluid is prepared in advance (i.e., 1 or 2 days) and stocked in a 60-l drum. The viscoplastic fluid used to-date is a stable polymeric gel (Carbopol Ultrez 10 provided by Gattefossé AG, Luzern, Switzerland). Polymer chains are mixed into a sodium-hydroxide/water solution at a given *p*H. This solution is left to rest for a long time so that all polymer chains have time to unroll and form a dispersion (repulsive interactions between chains). To ensure good light contrast, titanium dioxide (TiO_2) is added to whiten the Carbopol.
2. The fluid is gently poured into the reservoir, while the inclined plane is kept in the horizontal position. The material is then slowly mixed and its free surface is smoothed out by hand. The upper plane is then inclined at a given value and its position is checked using a laser-meter. A viscoplastic fluid does not flow if shear stresses are too low, which means that its free surface stays in the reservoir as it stood after pouring; there is no stress relaxation (due to viscoelasticity), nor creeping (due to viscosity), which would cause flattening of the free surface. This explains why the free surface needs to be smoothed before it is released and why it remains parallel to the plane nearly independently of the plane inclination.
3. Once all the devices are installed, the measurement system is calibrated, as explained at length in Sect. 6. A few minutes before starting the test, we collect a fluid sample and test it using a Bohlin CVOR rheometer to characterize its rheological properties.
4. We lift up the sluice gate and the material starts accelerating and flowing. The surge motion is imaged by the digital camera. When there is no significant motion, we stop recording images. The material is then removed from the flume and the plane is carefully cleaned.

3 Measurement system

3.1 How to measure the free-surface variations with time?

For dam-break experiments, the crux of the problem lies in properly measuring the free-surface evolution. Three criteria guided our choice among various systems. First, we needed a noninvasive system to avoid disturbing the free boundary. Second, global methods that are able to capture the flow surface within a single pass were preferred over scanning methods, which are not well suited to providing snapshots. Third, we wished to develop a method that would allow high acquisition rates.

The method chosen involved projecting patterns onto the fluid surface. This method is described in Sect. 3.2.

3.2 Projecting patterns

Measuring the shape of an object using pattern projection can be broken down into three steps:

1. a given pattern is projected onto an object;
2. the object surface is imaged into a camera under an angle of incidence that differs from the imaging direction; and
3. the surface height is retrieved from the image.

For the sake of simplicity, two parallel lines are projected onto a surface, as shown in Fig. 4 (Bateman et al. 2006).

The height difference Δh can be then expressed as

$$\Delta h = \frac{\Delta p}{\tan \alpha}, \tag{1}$$

where $\Delta p = p_p - p_a$ is the difference between p_p the projected lines onto the object and p_a the apparent line on the surface viewed by the camera; α is the angle between the projected lines and the camera. The distance p_p is measured in a plane containing the camera and the projector, and parallel to the reference surface. p_p could also be defined as the apparent line on the reference surface viewed by the camera.

This simple relationship emphasizes two points. First, the closer the projected lines p_p are, the greater the accuracy of Δh is. Second, the closer to 90° the angle α is, the better the accuracy of Δh is.

A problem with projecting lines is that any valuable information between two lines is lost. There is another technical problem related to the camera resolution: for two lines to be distinguished by the camera, there must be a minimum separation distance of three pixels, which imposes a lower bound on the accuracy of Δh according to Eq. 1.

3.3 Projecting fringes

Instead of isolated lines, we can project cosine fringe patterns. Information theory would say that we are replacing a 1-bit system with an 8-bit system. Moreover, instead of relating height to light intensity, we can link height to the fringe phase. The intensity observed at a given pixel (i,j) can be written as

$$I(i,j) = r(i,j)[A(i,j) + B(i,j)\cos\phi(i,j)], \tag{2}$$

where r is the reflectivity coefficient of the surface to be measured, A and B are called the background and modulation intensities, and ϕ denotes the phase. The phase varies within the interval $[0, 2\pi)$. The observed intensity I differs from the modulation intensity B. Ideally, we would like the background intensity A to be zero, but in practice this is not possible. Working with phase instead of intensity has the substantial advantage that altering surface reflectivity r does not influence the outcome.

We used an imaging system made up of a digital camera coupled with a synchronized micro-mirror projector working at a maximum rate of 48 Hz. The $1{,}000 \times 1{,}000$ px^2 CCD camera and the projector were synchronized by the frame grabber. The actual projection surface was 1.8×1.1 m^2.

The projector was made up of $1{,}024 \times 768$ micro-mirrors that oscillated between two positions and onto which light was projected from an LED; for one position, light was reflected through the projector lens, while for the other position, light was not reflected. It was a binary system: for a given pixel, light was switched on or off. An 8-bit gray level was achieved by changing the projection duration of each micro-mirror. The main advantage of a micro-mirror projector (MMD) lies in its capacity to instantaneously project a given pattern. As mentioned in Sect. 3.1, achieving high resolution in time and space requires global acquisition and projection.

The 8-bit camera grabbed images, which are characterized by an intensity ranging from 0 (deep black) to 255 (white). For the phase to be properly retrieved from an image, a narrow range of 30 gray values is sufficient.

At its maximum rate, the camera recorded an image within 20.7 ms, while the fringes were projected for 20.3 ms. A time lag of 0.1 ms separated two images. Special attention was paid to ensuring that projection occurred entirely within the acquisition time with no synchronization delay. The MMD is originally a 1-bit projection system, relative intensity is controlled by the projection duration and therefore any error (e.g., an error due to time discretization) may lead to significant errors in the post-treatment of images.

Capturing 48 images per second with a $1{,}000 \times 1{,}000$ px^2 camera (i.e., 48 MB/s) during time intervals as long as 10 min requires a CameraLink connection between the camera and the frame grabber. To store the huge quantum of data within a short interval of time, we integrated four hard disks in parallel into a RAID-0 system. Note that the acquisition program was entirely developed using LabView.

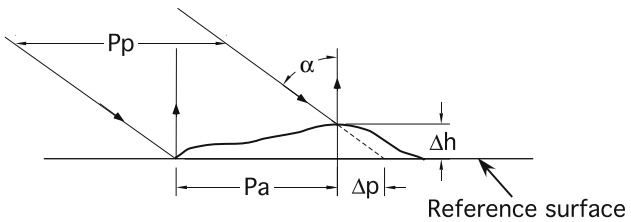

Fig. 4 Projection of parallel lines on a surface and the retrieved height

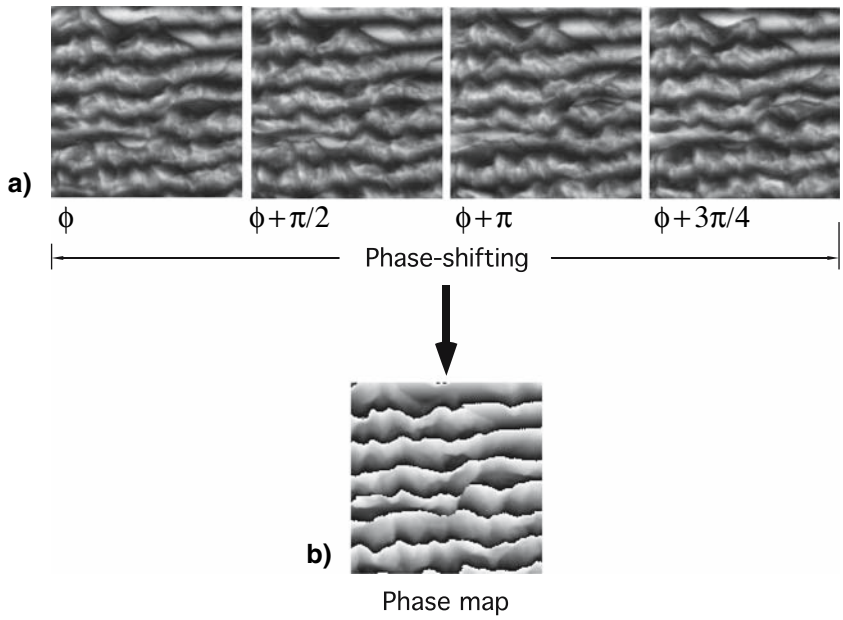

Fig. 5 Phase shifting: **a** with four images and **b** the resulting phase map

4 Phase mapping

The phase map is a graphical representation (density plot) of the $\phi(i,j)$ functions (see Eq. 2). Optic convention is used here: high values (2π) are in white, whereas lower values (0) are in black.

Most algorithms used for retrieving phase from an image or a series of images use one of the following methods: phase-shifting, Fourier transform (Takeda et al. 1982), local wave retrieval (Liebling et al, 2004), or wavelets. The first three methods are outlined in Sects. 4.1, 4.2, and 4.3, respectively. The phase map is also often referred to as the *wrapped phase*, which explains why we speak of unwrapping techniques when recovering flow depth from phase shift.

Note that to enhance accuracy, we must adapt our unwrapping algorithm with respect to fluid velocity. In the earlier moments of a run (typically 1–2 s), the flows accelerated vigorously and a one-image algorithm was used. After the flow had sufficiently slowed down, a three- or four-image algorithm was used.

Note also that for the phase map to be retrieved from the grabbed image(s), the images should not be saturated. If the grabbed images contained saturated pixels, this resulted in a loss of information and the creation of additional frequencies in the phase map.

4.1 Phase shifting

The principle of phase shifting consists in projecting $N \geq 3$ images of a fringe pattern shifted by $(i-1)2\pi/N$, with $i = 1,\ldots, N$ (Desmangles 2003). The phase can be analytically computed from the series of images using a least square approach. An example with a series of $N = 4$ images is given in Fig. 5, with the following intensities

$$\begin{cases} I_1(i,j) = A + B\cos\phi(i,j), \\ I_2(i,j) = A + B\cos\left(\phi(i,j) + \dfrac{\pi}{2}\right), \\ I_3(i,j) = A + B\cos(\phi(i,j) + \pi), \\ I_4(i,j) = A + B\cos\left(\phi(i,j) + \dfrac{3\pi}{2}\right), \end{cases}$$

where

$$\phi = f(I_1, I_2, I_3, I_4) = \arctan\frac{I_4 - I_2}{I_1 - I_3}. \quad (3)$$

A phase map can be extracted from any new image using the N–1 preceding images.

Three-fringe patterns can be projected at the same time using a red–green–blue (RGB) color coding. An independent phase map can be extracted from each new image. The idea is attractive, but requires a complicated and expensive setting (Jeong and Kim 2002).

The method based on three or four images is more appropriate when the fluid slows down and the relative motion between the first and the last images is less than 1 or 2 pixels. This method is not suitable at earlier times, when the fluid is released, because the displacement of the fluid between the first and the last images is too large. The resulting phase map is blurred and unusable. During the first instants of the test, the phase map must be

computed with only one image; this computation can be done with an FFT algorithm, as explained in Sect. 4.2, or with a local wave retrieval algorithm, as described in Sect. 4.3.

This method should be used as much as possible because it is the only one that gives the phase explicitly, whereas in other methods, the phase is established approximately by extrapolation.

4.2 Fourier transformation profilometry (FTP)

Fourier transformation profilometry (FTP) was first introduced by Takeda et al. (1982). The idea is to work in the frequency domain of the recorded images in order to filter out the projected frequency f_0 and keep only the desired frequencies ϕ_0 which contain the information on the object.

In FTP, one assumes that the variations of the background and modulation intensity A and B and the object frequency are slow compared with the projected frequency f_0.

Without loss of generality we fix that the projected frequency f_0 is in the i-direction only. Equation (2) is written as:

$$I(i,j) = a(i,j) + b(i,j)\cos[2\pi f_0 i\phi_0(i,j)], \tag{4}$$

where

$$a(i,j) = r(i,j)A(i,j)$$

and

$$b(i,j) = r(i,j)B(i,j).$$

Following Takeda et al. (1982) we obtain:

$$I(i,j) = a(i,j) + c(i,j)\exp(2\pi\imath f_0 i) + \bar{c}(i,j)\exp(-2\pi\imath f_0 i), \tag{5}$$

with

$$c(i,j) = \frac{1}{2}b(i,j)\exp[\imath\phi_0(i,j)] \tag{6}$$

where $\bar{c}$ denotes the complex conjugate of c.

Next, Eq. 5 is Fourier transformed with respect to i:

$$\hat{I}(f,j) = \hat{a}(f,j) + \hat{c}(f-f_0,j) + \hat{\bar{c}}(f+f_0,j), \tag{7}$$

where the hat symbol denotes the Fourier transforms, while f is the frequency in the i-direction.

$\hat{c}(f-f_0),j)$ is translated by f_0 toward the origin to obtain $\hat{c}(f,j)$ as sketched in Fig. 6. In our case f_0 is computed using a reference image (without ϕ_0).

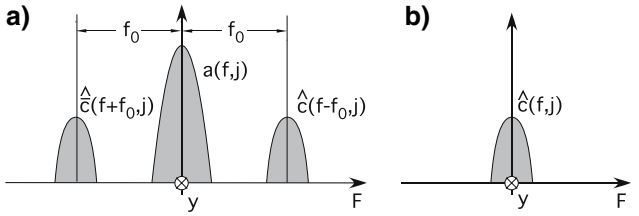

Fig. 6 Frequency map: **a** of a grabbed image, **b** with only the frequency of the projected cosine shifted to zero

$c(i,j)$ is then obtained by computing the inverse Fourier transform of $\hat{c}(f,j)$ with respect to f. The complex logarithm of (6) gives:

$$\log[c(i,j)] = \log\left[\frac{1}{2}b(i,j)\right] + \imath\phi_0(i,j). \tag{8}$$

The phase ϕ_0 of the object lies now in the imaginary part.

In the remaining subsection we explain how the FTP was implemented in our setup.

A cosine fringe pattern with 45° inclinations is projected onto the surface of the reference plane during the calibration procedure, as shown in Fig. 7a (see also Sect. 6). Two-dimensional Fourier transform analysis is then carried out on the recorded images as follows:

1. in the frequency map, the central peak is removed. This central peak represents frequencies close to zero, which are related to the inclined plane;
2. the frequency f_0 of projected patten is localized (see Fig. 7b);

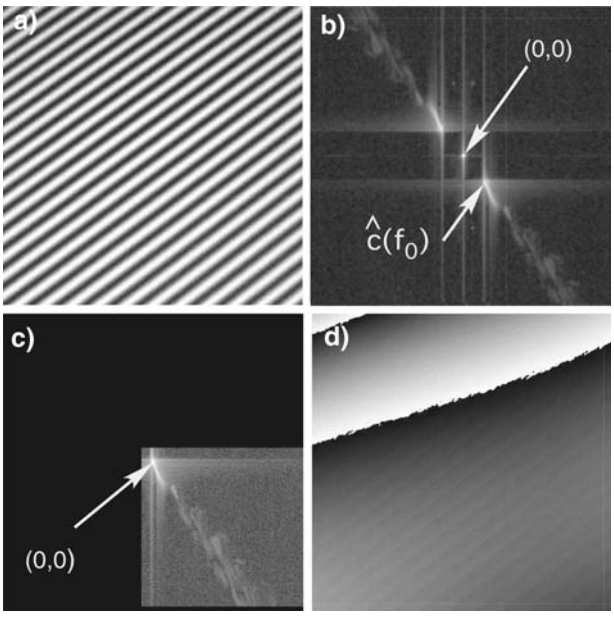

Fig. 7 Reference plane: **a** projected fringes, **b** image in FFT domain with the frequency f_O of the projected fringe, **c** image filtered and shifted and **d** reference plane phase map

3. the frequency map is filtered out to keep only the desired values (see Fig. 7c);
4. the frequency map is shifted from the frequency f_0 to the center (see Fig. 7c); and
5. an inverse FFT analysis is carried out on the frequency map. The argument of the (complex) inverse FFT output provides us with the phase map of the reference plane (see Fig. 7d).

Apart from the shift over f_0, this procedure is the same as the Hilbert transform. Indeed, in the last couple of years, the Hilbert transform has been used in interferometry to retrieve the phase from a single image (Onodera et al. 2005; Sticker et al. 2001; Larkin et al. 2001; Hitzenberger et al. 2001). The development of demodulation technique using the discrete Hilbert transform seems a promising method.

The same procedure is then repeated, during the test, with the recorded images except that the frequency map is shifted by the value f_0, which was computed during the calibration procedure. Figure 8 shows a typical example, which can be compared with the images obtained when using the reference plane (Fig. 7). The wrapped phase is then obtained by subtracting the new phase and the phase of the reference plane (see Fig. 8d). The resulting phase is the difference between the object phase and the reference-plane phase. Section 5.1 will show that unwrapping the difference between the object-phase and reference-phase maps is equivalent to taking the difference of the unwrapped phases.

Concerning point 1 in the description immediately above, a delicate point is to properly remove the central peak. Since it is present on every image, the simplest strategy to remove it is to normalize the intensity by subtracting the mean intensity, as follows

$$I = I_1 - \frac{1}{N}\sum_{n=1}^{N} I_n,$$

where I_i is the intensity of image i (i = 1,..., N) obtained during the calibration procedure (see Sect. 4.1) by shifting $N \geq 3$ fringe patterns by $(i–1)2\ \pi/N$.

Su and Chen (2001) discussed the influence of sampling in FTP. They emphasized that the recorded images as well as discrete Fourier Transform (DFT) are digital, whereas FTP theory is based on continuous Fourier transform. This difference between theory and experimental treatment induces errors at high frequency values. We are attempting to implement methods for reducing errors that arise at high frequencies; note that this issue remains of secondary importance in our context because the typical wavelength of the free surface is quite long in comparison with the wavelength related to these high frequencies.

The FTP efficiency depends a great deal on filtering, i.e., how many frequencies must be kept or discarded. An experienced user can easily find frequencies that must be removed in order to enhance map accuracy. Making this process automatic is, however, quite difficult. It is almost impossible to know in advance when a phase-shifting algorithm can be used as a replacement for FTP. To solve this problem, we project 45°-inclined fringes with a phase shift of $2(i–1)\ \pi/N$, with i = 1,..., N. Both phase-shifting and FTP algorithms can then be used depending on the quality of their respective phase map.

As illustrated in Fig. 9a, this method encounters serious problems when the projection pattern is parallel to a shadowed region. In this case, there is no real possibility to

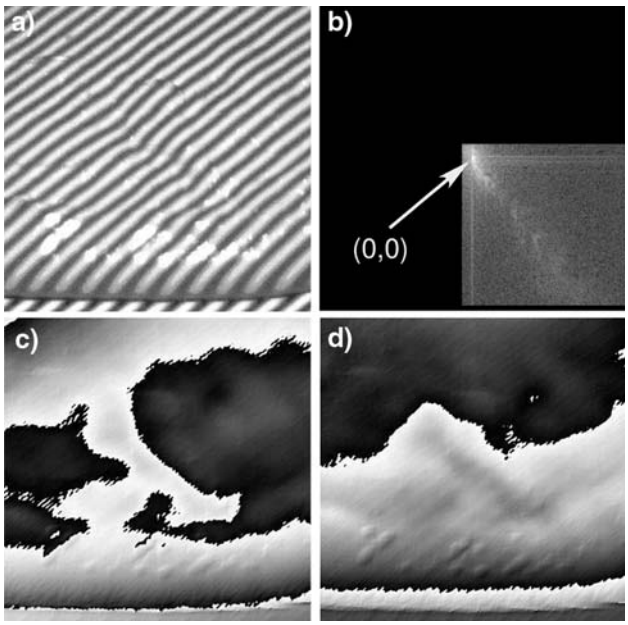

Fig. 8 Object: **a** projected fringes, **b** object image filtered and shifted in Fourier domain, **c** resulting phase map, and **d** difference between the object phase map and the reference plane phase map

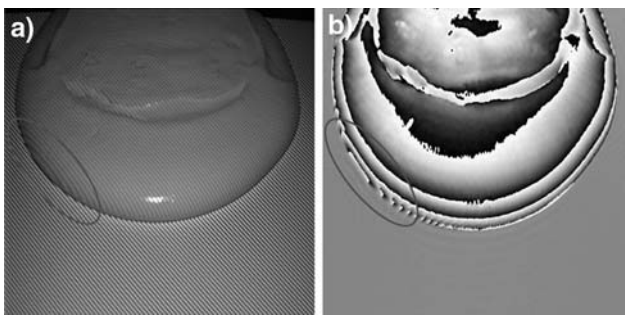

Fig. 9 Fringe projection at 45°: **a** grabbed image, **b** phase map computed with FTP. The phase map exhibits erroneous frequencies on the *bottom left corner* (area marked with the ellipsis)

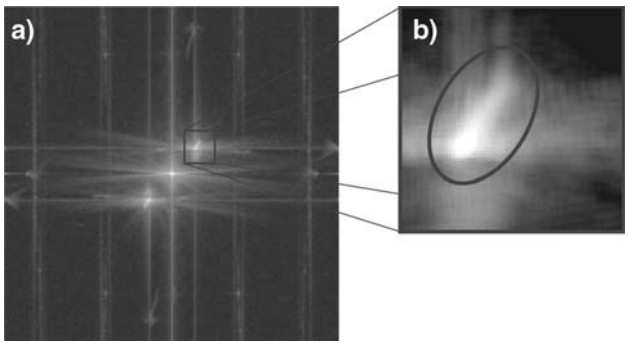

Fig. 10 Image in the FFT domain with the frequency f_0 of the projected fringe in a nontelecentric setup: **a** overview, **b** close-up of the diffuse peak f_0

differentiate a dark area arising from shadow from the dark area that results from the projection. Erroneous frequencies are introduced, which result in an incorrect wrapped phase, as highlighted in Fig. 9b. Furthermore, if the light pattern crosses the shadow area perpendicularly, the wrapped phase remains of fair quality. All the information contained in a shadowed region is lost (see Sect. 5).

In a nontelecentric setup (see Sect. 6), the fringe frequency changes with the incidence angle of the camera. The frequency f_0 is no longer represented by a sharp peak in the frequency map, but by something that is a bit more diffuse, as illustrated in Fig. 10.

4.3 Local wave retrieval

Different methods have been developed to date to retrieve the phase of a signal, using one image and a local algorithm. We decided to work with Liebling's algorithm (Liebling et al. 2004).

In local wave retrieval methods, one assumes that locally, only the value of the phase ϕ changes, while the background and modulation intensities A and B remain constant. The basic idea is then to divide an image into small windows and estimate the phase in each of those windows by assuming that, in a given window, only the phase ϕ changes. A two-dimensional bicubic spline function is fit to the intensity map, and we then interpret this function in terms of trigonometric functions to derive the phase. Empirically, one observes that results are improved when small phase steps and windows of sizes ranging from two to four wavelengths are used.

As for FTP, the resulting phase map is defined as the difference between the object-phase and the reference-phase maps.

A major advantage of this method lies in the fact that any image can be used as a reference image. As explained in Sect. 4.2, projecting fringes parallel to a shadowed region introduces errors in the wrapped phase. The influence of a shadowed region can be minimized using a projection pattern perpendicular to it. In our setup, a shadowed region appeared at the front of the surge. An ideal projection image would have patterns perpendicular to all shadowed areas. In our setup, a symmetric image was used, as shown in Fig. 11a. The axis of symmetry of the projection was aligned with the symmetry axis of the surge. This simple projection pattern tended to minimize the area where cosine fringe and shadow areas were parallel.

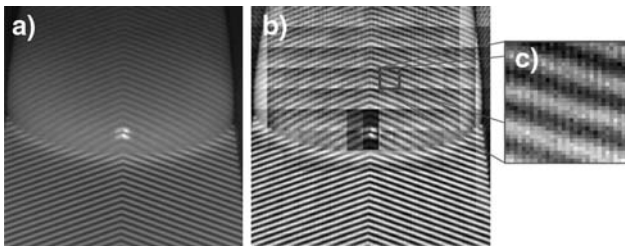

Fig. 11 **a** Grabbed image, **b** local wave retrieval using window, **c** close-up of one window

When this method is used with a symmetric projection, special attention should be paid to the calibration procedure because a sudden deviation in the unwrapped phase is likely to appear near the axis of symmetry (Fig. 12).

5 Phase unwrapping

Once we had obtained the phase map, we unwrapped it. The principle of phase unwrapping is quite easy to understand in one-dimensional problems. Let us consider that we have a phase signal ϕ defined over the interval $[0, 2\pi)$ and we want to unwrap it. Whenever the signal goes out from the interval $[0, 2\pi)$, we add or subtract 2π to it depending on the derivative $\partial_x\phi$, as shown in Fig. 13.

Without noise and shadow, phase unwrapping would have a single solution. Any unwrapping algorithm tends to

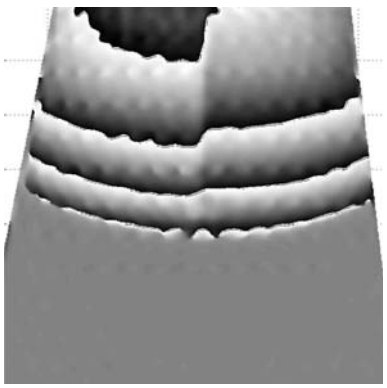

Fig. 12 Phase computed using the local wave retrieval algorithm

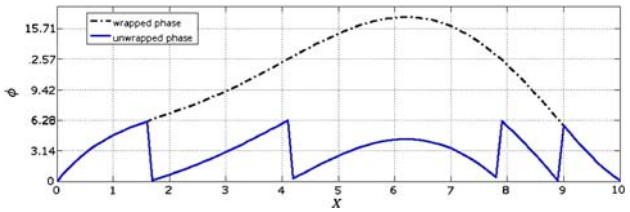

Fig. 13 Example of phase unwrapping in 1D

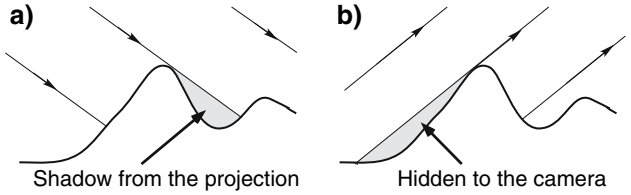

Fig. 15 **a** Shadow from the projector, **b** parts hidden from the camera

provide a proper approximate solution. The point is that noise blurs the sharp frontiers of the phase ϕ whenever ϕ approaches π (modulo π). Figure 14 shows a typical example of noise disturbance.

Ideally, to retrieve the phase ϕ from the observed intensity I (see Eq. 2), we would like to have the background intensity A equal to zero and the modulation intensity B equal to 255 (for an 8-bit system). In practice, B varies between 30 and 120. In order to increase B, two solutions are available:

- the acquisition time is increased so that more light is received by the camera; or
- the gain of the camera is increased to make it more light-sensitive.

In both cases, noise is increased. Indeed, when taking an image, a camera records the trajectory of the filmed object. If the displacement is relatively short, the picture looks sharp. In the converse case, if the typical displacement length exceeds three pixels, the image is blurred. In the latter case, the reconstructed phase is noisy. In short, we have two alternatives:

- if the acquisition time is long enough, the recorded image is blurred, but the modulation intensity B is relatively high; or
- if the acquisition time is short, the resulting image is sharp, but at the same time is characterized by lower B values.

A tradeoff must be found. To obtain high modulation intensity B while keeping a short acquisition time, we can increase light intensity or increase the gain of the camera. The camera gain is increased by increasing the gain of the charge amplifier, so that fewer photons are needed to capture an image. However, this is at the expense of an increased noise level.

Shadowed regions appear when the plane surface is not entirely covered by the projected image or when part of this surface is hidden to the camera, as sketched in Figs. 15 and 16. All the information in the shadowed or hidden parts is lost. In order to obtain high-quality results, care must be taken to avoid such regions, while trying to keep the angle between the projecting and the acquiring directions as close as possible to 90°. Again, a compromise must be found between the extent of shadowed areas and the mismatch of incidence angles.

To date, different methods can provide approximations to two-dimensional unwrapping problems. For instance, the book of Ghiglia and Pritt (1998) reviewed different approaches to phase unwrapping and provided eight C++ routines illustrating these strategies. On the whole, there are two different approaches to phase unwrapping: one is based on path-following methods or local methods, while the other is based on minimum-norm methods or global methods. The path-following method starts at a given point in the phase map and computes the neighboring points by following a predefined path. The main problem arises in choosing the best path to avoid shadowed or noisy parts. Minimum-norm methods minimize the integral of the square difference between the gradients of the solution and the path obtained using different strategies. The square difference can be weighted by different functions.

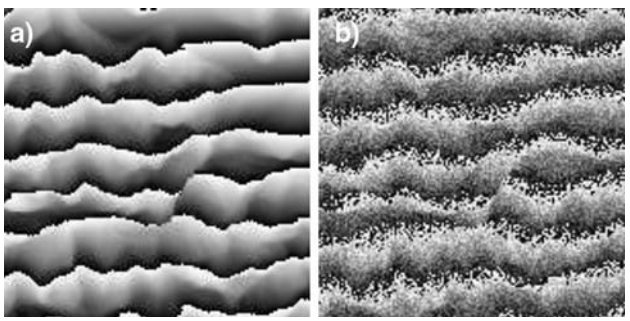

Fig. 14 Phase map: **a** original; **b** with noise

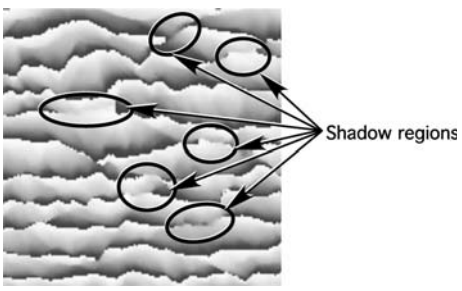

Fig. 16 *Shadow regions* on an image

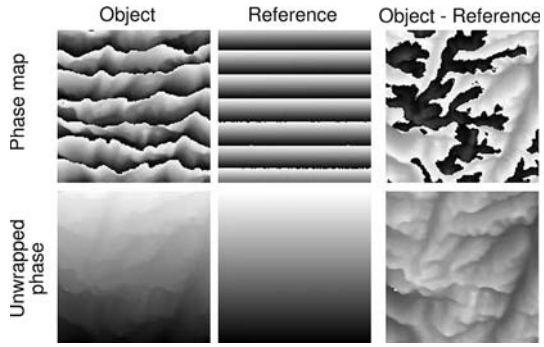

Fig. 17 Unwrapping the difference of the object phase map and the reference phase map is equal to the difference of the unwrapped phases

5.1 Phase difference

A good way to reduce computation time is to unwrap the difference of the two phase maps instead of computing the difference of the respective unwrapped phase, as shown in Fig. 17. The resulting map shows fewer 2 π jumps, which makes reconstructing the unwrapped phase easier, faster, and more accurate. Unwrapping the difference of the object phase map and the reference phase map provides the same results as taking the difference of the unwrapped phases.

6 Calibration

The calibration procedure computed a matrix $M_{ij\varphi}$ to transform the image pixels i,j and the unwrapped phase φ into a metric Cartesian coordinates system x,y and a height z, respectively.

Equation (1) gives the height as a function of the angle α and the distance between two lines P_p. The following assumption underlies this equation: projection and acquisition must be telecentric, which is not the case in our setup (Chen and Quan 2005).

Theoretically, knowing the relative position of the camera, the projector, and the inclined plane as well as the projection and camera angles make it possible to modify Eq. 1 by including a height correction factor for each position (Desmangles 2003). This method involves accurately measuring the position of each element of the setup, which is time-consuming. Moreover, it does not take optical deformation into account. For these reasons we decided to use a more practical calibration procedure, which was based on a modified version of the virtual calibration-plane method proposed by Xiaoling et al. (2005).

The underlining idea of the calibration procedure is to position a calibration plate at different height z and project the pattern to be used during the test. Each image of the calibration plate gives a relation between the pixel i,j and the Cartesian coordinate system x,y and a relation between the computed phase ϕ and the height z.

To calibrate this measurement system, we proceeded as follows:

1. Well-defined patterns such as squares were projected onto the inclined plane to adjust the focus of the projector and camera.
2. We checked that the recorded images from the camera properly included the zone of interest. Light power and projection resolution were optimized by fitting the size of the projected images with the plane size.
3. We related the Cartesian coordinates x,y,z of the plane with a grid i,j; each cell representing a pixel of the unwrapped phase. To that end, we designed a calibration plate, i.e., a simple plane surface, over which we marked gray disks 2 cm in diameter spaced 10 cm apart. The upper surface of this plane corresponded to elevation $z_0 = 0$. All fringe patterns, which were used in experimental runs, were then projected on this calibration plane. The modulation of the reference plane was obtained by averaging the calibration projections, while the position of the circle centers were found using a least-square method.
4. The wrapped phase was referred to as ϕ_{z_0}. A relation between the plane xy_{z_0} and the camera coordinates ij was obtained using a piecewise linear interpolation.
5. Any circle that was partially contained in the image was removed because its center could not be accurately located (information was partly lost). If it were kept, it would introduce distortion.

The same procedure was repeated k times with the calibration plate placed over the inclined plane at an elevation z_k, with $k = 1,2,...,K$; in practice, we used K values as high as 7. A relation between the plane $xy_{z_k}(k = 1, 2, \ldots, K)$ and the camera coordinates ij was obtained using a piecewise linear interpolation. The corresponding wrapped phase ϕ_{z_k} was computed and the phase difference $\phi_{z_k} - \phi_{z_0}$ was unwrapped and denoted by φ_{z_k}. Note that φ_{z_k} was not unique since $\phi_{z_k} - \phi_{z_0} \in [0, 2\pi)$. z_k was a function of $\varphi_{z_k} = \psi_{z_k} + j\pi$, with $j = 1,2,....$ A way of finding j is explained in Sect. 6.1. Once $\phi_{z_k} = \varphi_{z_k} + j\pi$ was defined, a piecewise linear interpolation method was used to complete z-axis calibration. The unwrapped phases φ_k ($k = 1,2,...,K$) at elevation z_k ($k = 1,2,...,K$) were considered as reference phases. Based on the reference phases and their elevations z_k, every pixel height (z-axis coordinate) was obtained by linearly interpolating φ_k and z_k.

We ended up with a calibration matrix $M_{ij\varphi}$, which related the value of the unwrapped phase φ_k in the pixel coordinate system ij with the elevation z_k in the plane coordinate system xy. Figure 18 shows the matrix $M_{ij\varphi}$ with five surfaces φ_k, which represented five different

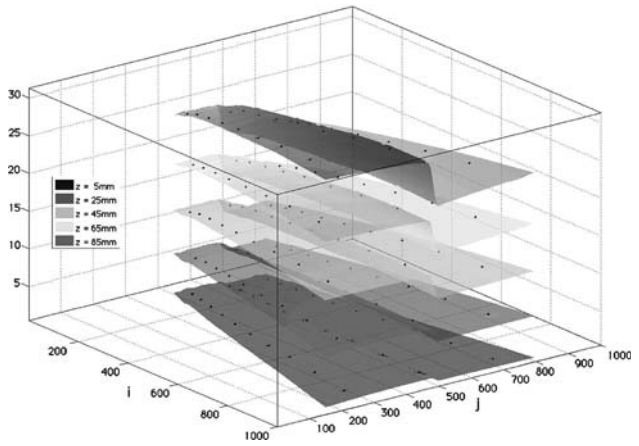

Fig. 18 Calibration matrix $M_{ij\phi}$ with five reference planes z–k. The *dots* represent the position of the circle centers on the calibration plane

elevations z_k: 5, 25, 45, 65, and 85 mm. The dots represent the position of the circle centers located on the calibration plane.

The steps, which appear in the middle of each surface φ_k, result from a symmetric projected pattern, which was not aligned with the x- or y-direction of the calibration plane. For the camera, the projection angles on either side of the symmetry axis were different, which led to contrasted sensitivity to flow depth (see Eq. 1). A closer look at Fig. 19a shows that the axis of symmetry of the projected pattern was not vertical; the projection angle was slightly different on either side of that line. This leads to a step-shaped variation in the phase map (see Fig. 19b) as well as in the unwrapped phase map (see Fig. 19c). As expected, the calibration process resulted in the surface not showing any step (Fig. 19d).

Compared to classical ways of calibration, this method reduces the hardware requirement of the system. It also simplifies the process of grabbing and processing data. Better accuracy is achieved by increasing the number of virtual calibrating planes z_k. The standard deviation error, using five virtual planes, is in the order of 1%.

6.1 Temporal phase unwrapping

A problem arose with our setup: two calibration planes with two different heights may still have the same phase ϕ_{z_k}. To get around this problem, we use temporal phase unwrapping (TPU). This technique is presented at length by Huntley and Saldner (1997). It involves unwrapping a phase with high sensitivity by means of other phases with lower sensitivity.

First, a series of phase-shifted images (see Sect. 4.1) is projected with a projected wavelength p_{p1}, which is longer

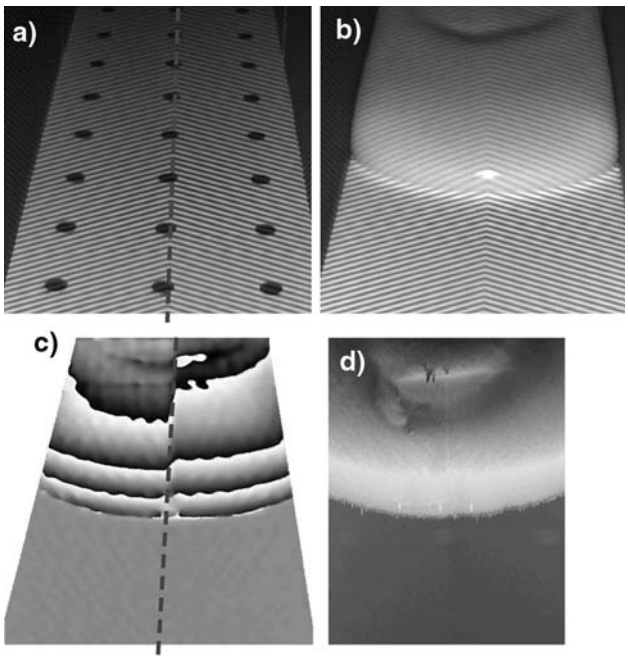

Fig. 19 Projection of a symmetric pattern not aligned with the reference plane; **a** grabbed image of the reference plane with the axis of symmetry in the dotted line, **b** grabbed image of the sluice, **c** phase map with a step on the axis of symmetry, **d** the resulting surface without any step

or equal to the plane length. In this case, the phase ϕ_1 is equal to the unwrapped phase φ_1. The unwrapped phase φ_1 is contained within the interval $[0, 2\pi)$ and the accuracy of the measure is low. We know from Eq. 1 that the measurement accuracy can be increased when a series of images is projected with a smaller wavelength. We chose to project a second series of phase-shifted images, but with a wavelength p_{p2} set to half the length p_{p1}, having twice the accuracy, the unwrapped phase φ_2 is contained in the interval $[0, 4\pi)$. To avoid complex unwrapping algorithms (see Sect. 5) to compute φ_2, we use the TPU method:

1. ϕ_1 is computed from the first series of phase-shifted images: $\phi_1 = \varphi_1 \in [0, 2\pi)$;
2. φ_1 is multiplied by 2 and the result is denoted by ψ_1. ψ_1 belongs to the interval $[0, 4\pi)$;
3. ϕ_2 is computed from the second series of phase-shifted images. $\phi_2 \in [0, 2\pi)$;
4. the unwrapped phase φ_2 is directly calculated by adding 0 or 2π to ϕ_2 so that $\phi_2 + (0 \text{ or } 2\pi) = \psi_1 + \varepsilon$. ε is the residual error: $\varphi_2 = \psi_1 + \varepsilon$.

Once that φ_2 is computed, the wavelength of a new series of phase-shifted images with a wavelength p_{p3} is set to half the length p_{p2}. The accuracy of the new unwrapped phase φ_2 lies within the interval $[0, 8\pi)$. This processes can be repeated n times until the desired accuracy is reached, as illustrated by Fig. 20.

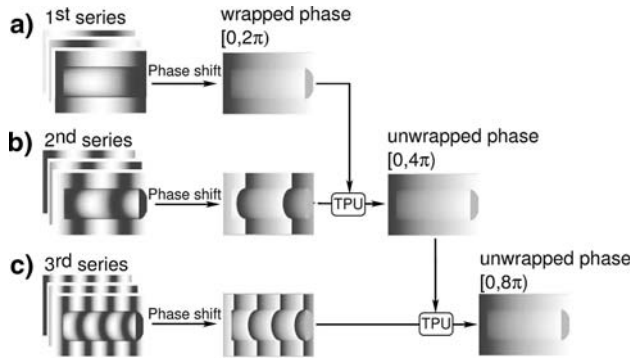

Fig. 20 Temporal phase unwrapping. **a** A series of phase-shifted images is projected with a projected wavelength P_p1 longer or equal to the plane length. ϕ_1 is equal to the unwrapped phase φ_1. **b** A second series of phase-shifted images is projected, but with a wavelength P_{p2} set to half the length P_{p1}. ϕ_2 is computed. The unwrapped phase φ_2 is directly calculated by adding 0 or 2π to ϕ_2 so that $\phi_2 + (0 \text{ or } 2\pi) = 2\,\phi_1 + \varepsilon$. **c** This process is repeated with a new series of images

6.2 Computational time

The mean time spent from acquiring an image to obtaining a three-dimensional surface takes nearly 5 min on a Dual-Core Intel Xeon processor at 2.66 GHz:

- on average, a one-image algorithm for retrieving the phase takes 1'30" (see Sects. 4.2, 4.3);
- phase unwrapping takes 1 to 2 min depending on the complexity of the object phase (see Sect. 5);
- transforming the unwrapped phase map into an image in a Cartesian coordinate system takes about 1.5 min, depending on the number of virtual planes z_k used (see Sect. 6).

Given that a typical experimental test lasted at least 1 min (usually from 1 min to 1 h) and we operated a camera at 45 fps, we ended up with a minimum of 2,700 images. The total computational time would be 225 h (9.5 days), which would make the method of limited interest when conducting many experiments. In order to speed up calculation, we used the *Distributed Computing Toolbox* from Matlab, with a grid of 21 CPUs, which made it possible to reduce the computational time to 12 h.

7 Example

Here, we provide the results obtained when releasing a 40-l volume of Carbopol Ultrez 10 at a solid concentration of 0.3% down a 30-cm wide channel. The bed inclination was 12° with respect to the horizontal and the channel cross-section was rectangular.

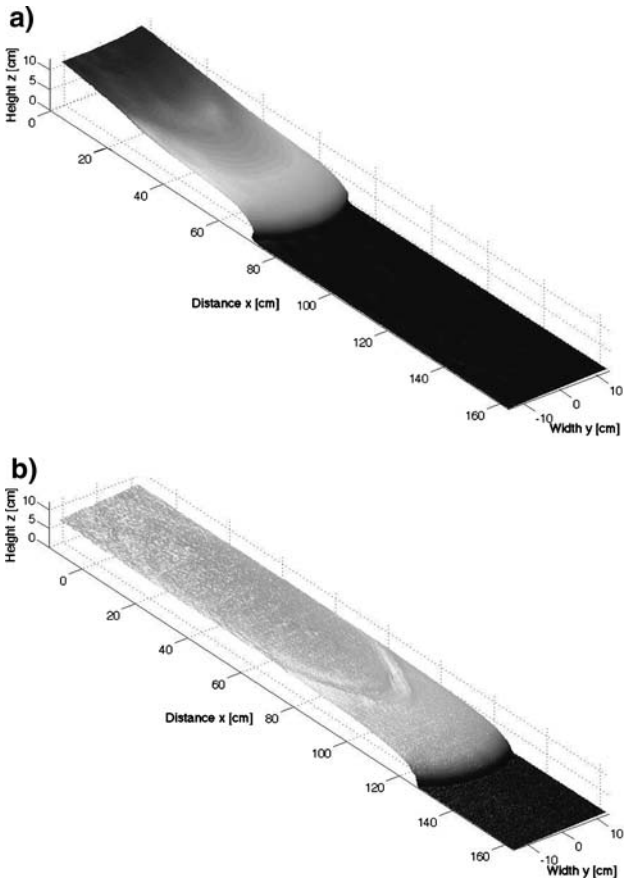

Fig. 21 Free surface at **a** $t_1 = 1.0$ s, **b** $t_1 = 52.0$ s

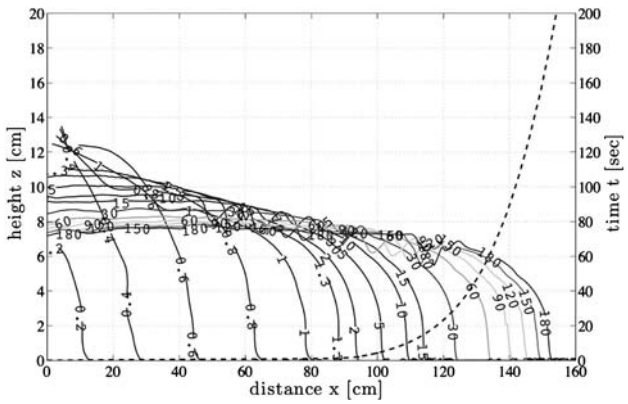

Fig. 22 Flow-depth profile (measured at the centerline) of the surge (*continuous lines*) and position of the front in function (*dash line*) of the time for a visoplastic fluid with a yield stress of 86 Pa

Figure 21a represents the grabbed image of the flow taken at time $t_1 = 1$ s. The wrapped phase was obtained by a local wave retrieval algorithm. Figure 21b illustrates the same flow but at time $t_2 = 52.0$ s. The phase was computed using a 4-image algorithm.

Figure 22 presents the variation in the flow-depth profile (at the centerline) and front position over time. These two

sets of data are used to compare different flow configurations with different materials. In this example, the position of the front reached 80 cm in 1 s due to its inertia and then dramatically slowed down to reach 140 cm in more than 90 s.

8 Conclusion

In order to accurately measure the three-dimensional flow depth profiles in the dam-break problem, a new experimental facility and procedures have been built.

Three-dimensional flow-depth profiles are measured using a high-speed digital camera, which records how a fringe pattern projected onto the flow surface is deformed. Even if this technique is not new and has been used in different fields, it has never been used to measure large moving objects such as a surge down an inclined plane. Many innovative solutions have been developed to sort out the numerous technical problems that arise when a fast and deformable material flows. Various methods, algorithms, and techniques ranging from airborne Synthetic Aperture Radar to biomedical imaging have been combined to obtain a high-accuracy measurement system.

Our system allowed us to measure the surface height of a 1.8×1.1 m^2 surge with an uncertainty in the order of 1 mm at a frame rate of 48 Hz. With this tool, we think that we can acquire high-accuracy data related to the dam-break problem, which can then be used to test the various numerical models developed to compute the spreading of a non-Newtonian material in time-dependent flow conditions.

Acknowledgments The work presented here was supported by the Swiss National Science Foundation under grant number 200021-105193/1, the competence center in Mobile Information and Communication Systems (supported by the Swiss National Science Foundation under grant number 5005-67322), and specific funds provided by EPFL (vice-présidence à la recherche).

References

Bartelt P, Salm B, Gruber U (1999) Calculating dense-snow avalanche runout using a voellmy-fluid model with active/passive longitudinal straining. J Glaciol 45:242–254

Bateman A, Granados A, Medina V, Velasco D, Nalesso M (2006) Experimental procedure to obtain 2d time-space high-speed water surface. In: Ferreira R, Alves E, Leal J, Cardoso A (eds) River flow 2006. Balkema 2:1879–1888

Chen L, Quan C (2005) Fringe projection profilometry with nonparallel illumination: a least-squares approach. Opt Lett 30(16):2101–2103

Desmangles AI (2003) Extension of the fringe projection method to large objects for shape and deformation measurement. PhD Thesis, EPFL

Eaket J, Hicks F, Petersen A (2005) Use of stereoscopy for dam break flow measurement. J Hydraul Eng 131:24–29

Ghiglia DC, Pritt MP (1998) Two-dimensional phase unwrapping: theory, algorithms, and software. Wiley-Interscience, Wiley, cop.

Griffiths R (2000) The dynamics of lava flows. Annu Rev Fluid Mech 32:477–518

Hitzenberger CK, Sticker M, Leitgeb R, Fercher AF (2001) Differential phase measurements in low-coherence interferometry without 2π ambiguity. Opt Lett 26(23):1864

Hogg A, Pritchard D (2004) The effects of hydraulic resistance on dam-break and other shallow inertial flows. J Fluid Mech 501:179–212

Huang X, García M (1997) A perturbation solution for bingham-plastic mudflows. J Hydraul Eng 123:986–994

Huntley JM, Saldner HO (1997) Shape measurement by temporal phase unwrapping: comparison of unwrapping algorithms. Meas Sci Technol 8:989–992

Iverson R (1997) The physics of debris flows. Rev Geophys 35:245–296

Iverson R, Logan M, Denlinger R (2004) Granular avalanches across irregular three-dimensional terrain: 2. experimental tests. J Geophys Res 109:F01015

Jeong MS, Kim SW (2002) Color grating projection moiré with time-integral fringe capturing for high-speed 3-d imaging. Opt Eng 41(8):1912–1917

Larkin KG, Bone DJ, Oldfield MA (2001) Natural demodulation of two-dimensional fringe patterns. i. general background of the spiral phase quadrature transform. J Opt Soc Am A 18(8):1862

Liebling M, Blu T, Unser M (2004) Complex-wave retrieval from a single off-axis hologram. J Opt Soc Am A 21(3):367–377

Onodera R, Watanabe H, Ishii Y (2005) Interferometric phase-measurement using a one-dimensional discrete hilbert transform. Opt Rev 12(1):29–36

Parker G, Fukushima Y, Pantin H (1986) Self-accelerating turbidity currents. J Fluid Mech 171:145–181

Pouliquen O, Forterre Y (2002) Friction law for dense granular flow: application to the motion of a mass down a rough inclined plane. J Fluid Mech 453:133–151

Pritchard D (2005) On fine sediment transport by a flood surge. J Fluid Mech 5343:239–248

Ritter A (1892) Die fortpflanzung der wasserwellen. Zeitschrift des Vereines Deutscher Ingenieure 36(33):947–954

Saint Venant B (1871) Théorie du mouvement non permanent des eaux, avec application aux crues des rivières et à l'introduction des marées dans leur lit. Comptes Rendus de l'Académie des Sciences, série I 173:147–154– 237–240

Sticker M, Hitzenberger CK, Leitgeb R, Fercher AF (2001) Quantitative differential phase measurement and imaging in transparent and turbid media by optical coherence tomography. Opt Lett 26(8):518

Su X, Chen W (2001) Fourier transform profilometry: a review. Opt Lasers Eng 35:263–284

Takeda M, Ina H, Kobayashi S (1982) Fourier-transform method of fringe-pattern analysis for computer-based topography and interferometry. J Opt Soc Am 72(1):156–160

Xiaoling Z, Yuchi L, Meirong Z, Xiaobing N, Yinguo H (2005) Calibration of a fringe projection profilometry system using virtual phase calibrating model planes. J Opt A Pure Appl Opt 7:192–197